https://doi.org/10.5194/egusphere-2026-3173
Preprint. Discussion started: 11 June 2026

A preliminary analysis of tropical anvil-cloud dynamics from EarthCARE

Hirohiko Masunaga[1]

[1]Institute for Space-Earth Environmental Research, Nagoya University, Nagoya, Japan

Correspondence: Hirohiko Masunaga (masunaga@nagoya-u.jp)

Abstract. The vertical motion in tropical anvil clouds is crucial for understanding their maintenance and evolution but is notoriously difficult to observe. This work explores the potential utility of EarthCARE in revealing previously unobserved aspects of anvil clouds using the radar-only (2A.CPR_CLP) and radar-lidar synergy (2B.AC_CLP) products. Composite vertical profiles of cloud fraction sorted by ice water path (IWP) are found to represent a smooth transition from deep convection to anvil and thin cirrus clouds. In-cloud vertical air motion as estimated from Doppler measurements reveals that intense updraft penetrating within deep convection gives way to a weaker ascent in anvil clouds. The CPR-only product slightly underestimates the ascent in anvil clouds relative to the CPR-ATLID product due to a difference in the particle size distribution, while the overall spatial pattern of vertical air motion remains consistent. Diagnostic horizontal wind is then derived from the vertical motion estimates under mass conservation in composite vertical-horizontal space. The resulting wind vector field emerges as an overturning mesoscale circulation constituted of a mid-tropospheric inflow and an upper-tropospheric outflow. The present findings, although preliminary, confirm the promising potential of EarthCARE observations for investigating the anvil cloud dynamics.

1 Introduction

Clouds prevail in the upper troposphere over the Tropics. While the high-cloud amount is about 37% when averaged over the globe, this number increases by 10% at tropical latitudes (Stubenrauch et al., 2024). Tropical high clouds consist of at least two distinct components differentiated from each other by formation mechanism. In situ cirrus is formed ubiquitously in the tropical tropopause layer (TTL) owing to very low temperature there leading to a high relatively humidity, and also because of the limited moisture availability in TTL that prevents ice crystals from growing fast enough to fall out quickly (Jensen et al., 1996; Fueglistaler et al., 2009).

Another member of tropical cirrus is anvil clouds formed in association with the detrainment of condensate from deep convection, which accounts for nearly one half of all the tropical cirrus (Massie et al., 2002; Luo and Rossow, 2004). An anvil cloud can by far outlive the deep convection that produced it, maintained over a length of time depending on different factors such as radiatively-driven in-cloud dynamics (Ackerman et al., 1988; Lilly, 1988; Hartmann et al., 2018; Gasparini et al., 2019), cloud microphysics (Jensen et al., 1996; Garrett et al., 2005; Ohno et al., 2021), and dynamic and thermodynamic environments in the upper troposphere (Sherwood, 1999; Hartmann and Larson, 2002; Bony et al., 2016; Seeley et al., 2019) and even through the lower tropospheric dynamics (Masunaga and Bony, 2018; Masunaga, 2023).

Global observations of the cloud radiative and microphysical properties are invaluable for translating the process-level knowledge to understand the working of cloud feedback as part of Earth's climate system. Global measurements of the anvil cloud properties benefit particularly from active remote sensing from space with the ability to vertically profile the in-cloud structure. The CloudSat and Cloud-Aerosol Lidar and Infrared Pathfinder Satellite Observations (CALIPSO) satellites, flying in formation for over 15 years since their launch in 2006 (Stephens et al., 2018), opened a new pathway to study the cloud vertical structure with simultaneous radar and lidar measurements. CloudSat-CALIPSO data have been demonstrated to be instrumental in studying anvil cloud dynamics (e.g., Sokol and Hartmann, 2020; Wall et al., 2020; Horner and Gryspeerdt, 2023).

While CloudSat and CALIPSO ended their missions in 2023, the Earth Clouds, Aerosols and Radiation Explorer (EarthCARE) satellite was sent into orbit in 2024, carrying Cloud Profiling Radar (CPR) and Atmospheric Lidar (ATLID) with other two instruments aboard (Illingworth et al., 2015; Wehr et al., 2023). EarthCARE CPR (EC-CPR) is a W-band Doppler radar designed to measure the vertical velocity of hydrometers as well as their back-scattered echo. ATLID is a high spectral resolution lidar (HSRL) transmitting ultraviolet (355 nm) laser pulses, having the advanced capability to separate out molecular scattering signals from the particle scattering echoes from clouds and aerosols. As such, EarthCARE not only succeeds to CloudSat and CALIPSO over an extended period of time but benefits from enhanced technologies in spaceborne radar-lidar observations.

Vertical velocity remains among key uncertainties in the formation and maintenance mechanisms of cirrus clouds (Kärcher and Spichtinger, 2009). Difficulties arise largely, if not entirely, from the lack of vertical motion measurements in upper-tropospheric clouds to verify existing hypotheses and model simulations (Gasparini et al., 2023). EarthCARE brought about breakthrough as the first spacecraft carrying a Doppler weather radar. Early observations from EC-CPR so far have already proven the value of Doppler measurements for studying the vertical motion in vigorous convective systems (Galfione et al., 2025; Roh et al., 2025; Aoki et al., 2026; Hotta et al., 2026) and the microphysics in cirrus clouds (Seiki et al., 2025).

The potential of EarthCARE, however, has yet to be explored with focus on anvil clouds. Vertical air velocity in anvil clouds remains within $\pm 1\ \mathrm{m}^{-1}$ most of the time (Muhlbauer et al., 2014), which can be largely or more than entirely offset in Doppler measurements by the contribution of hydrometeor sedimentation. Reliable Doppler estimation of vertical air motion would require a careful treatment of the algorithmic assumptions on cloud microphysics for properly factoring out the sedimentation component. It is crucial to assess if Doppler observations provide a reasonable diagnosis of vertical air velocity as recorded in the EarthCARE data products.

The goals of this paper are twofold. First, the vertical motion estimates are examined for robustness in light of the archetypical cloud-system structure comprised of a deep convective tower and anvil clouds (Section 3.2). This is done by averaging observations into a two-dimensional composite diagram in the IWP-height plane. The radar-only product is then compared against the radar-lidar synergy product in composite space. The difference between the two products provides a measure of minimum uncertainty in the EarthCARE measurements of cloud properties and vertical air motion, as will be detailed in Section 3.3. Second, a diagnostic estimate of horizontal wind is derived from vertical velocity to illustrate two-dimensional wind

https://doi.org/10.5194/egusphere-2026-3173
Preprint. Discussion started: 11 June 2026

field in the vertical plane (Section 4). This is a preliminary experiment intended to illuminate the unexplored potential of EarthCARE for looking into the dynamics of anvil clouds.

2 Data

2.1 EarthCARE data products

The EarthCARE mission was developed and is being operated jointly by Japan Aerospace Exploration Agency (JAXA) and European Space Agency (ESA). Two independent sets of the EarthCARE science data products are produced and distributed by JAXA and ESA (Eisinger et al., 2024). This work analyzes the cloud fraction (the number of cloudy pixels divided by the total pixel count), ice water content (IWC), ice water path (IWP), cloud effective radius, Doppler velocity, the terminal velocity of hydrometeors, and in-cloud vertical air velocity from the JAXA standard Level-2 cloud products of 2A.CPR_CLP vBb (CPR-only) and 2B.AC_CLP vBb (CPR-ATLID synergy) (Sato et al., 2025). These products contain two sets of variables having different spatial resolutions reconstructed with 1- and 10-km horizontal integration along the satellite track. The 10-km product is chosen for the current analysis to ensure a desirable Doppler accuracy within $\sim 0.3\,\mathrm{m\,s^{-1}}$ (Hagihara et al., 2023). The vertical resolution of CPR is 500 m but is oversampled every 100 m. The CPR-ATLID synergy product has the same horizontal and vertical sampling intervals as the CPR-only product.

All EarthCARE observations over the global tropical oceans (i.e., all longitudes for 20°S-20°N with landmasses and islands removed) are analyzed for the 14-month period from the beginning of August 2024 to the end of September 2025. The latest product version (vCb) released for 2A.CPR_CLP and 2B.AC_CLP is not adopted here because ample statistics are difficult secure due to a limited length of record. The version vCb is so far available only for very recent months since the release date, still pending for reprocessing back in time at the moment of this writing.

2.2 Doppler velocity measurements and vertical motion estimates

Doppler velocity, w_D, measured by a vertically pointing radar is related to in-cloud vertical motion as

$$w_D = w_{t,Z} + w_{a,c} + \varepsilon, \qquad (1)$$

where $w_{t,Z}$ is the terminal velocity of hydrometeors with respect to air (or sedimentation velocity) weighted with the radar back-scattering coefficient in the integral over particle size, $w_{a,c}$ denotes in-cloud vertical air velocity, and ε summarizes the measurement and retrieval errors. By design, w_D would offer a good proxy of terminal velocity in still air ($w_{a,c} = 0$), with the caveat that the fall velocity of large particles predominates as radar back-scattering is acutely sensitive to particle size. In contrast, w_D could be a large positive (ascending) in intense convective towers where $w_{a,c}$ overwhelms $w_{t,Z}$ in magnitude. It is otherwise not an obvious task to separate $w_{t,Z}$ from $w_{a,c}$ in a measurement of w_D.

An existing method to evaluate $w_{a,c}$ from Doppler observations is to isolate out $w_{t,Z}$ by applying temporal averaging to w_D (e.g., Orr and Kropfli, 1999; Deng and Mace, 2006; Protat and Williams, 2011). The approach is based on the premise that vertical air motion with a certain horizontal scale may be temporally averaged out over an adequate time interval while the

https://doi.org/10.5194/egusphere-2026-3173
Preprint. Discussion started: 11 June 2026

sedimentation speed is not (Mace et al., 2002). The algorithm to derive particle sedimentation velocity is built upon this line of studies for ESA's EarthCARE products (Kollias et al., 2023).

An alternative strategy was proposed by Sato et al. (2009) that does not involve any averaging procedure but instead relies on an explicit characterization of cloud microphysics in separating $w_{t,Z}$ from $w_{a,c}$. JAXA's EarthCARE datasets analyzed in this work (2A.CPR_CLP and 2B.AC_CLP) are built upon this method. Their cloud microphysical model allows for a bimodal particle size distribution (PSD) to account for large precipitating ice (snow and graupel) and co-existing tiny ice crystals. The adequate PSD determined to match a given CPR-ATLID or CPR-only observation (Sato and Okamoto, 2011) is applied to the calculation of $w_{t,Z}$, with which $w_{a,c}$ is obtained through Eq. (1). The same PSD model is used for the deconvolution of $w_{t,Z}$ into w_t, the latter of which denotes the PSD-weighted, but *not* reflectivity-weighted, terminal velocity as stored in the 2A.CPR_CLP and 2B.AC_CLP products. More technical aspects of the algorithm design are described in Sato et al. (2025) and the algorithm theoretical basis document (ATBD) (Nakajima et al., 2026).

The major sources of Doppler measurement errors, ε in Eq. (1), include Doppler velocity folding, multiple scattering, mirror image echoes, and antenna mispointing errors. Doppler velocity folding or aliasing occurs when the the target's speed exceeds the Nyquist velocity, proportional to the pulse repetition frequency (PRF) of the radar for a given electromagnetic frequency. The EC-CPR has three observation modes with different PRFs and, resultingly, different maximum observable altitudes of 16, 18, and 20 km (Imura et al., 2026). A higher PRF ensures a smaller Doppler noise and a larger Nuquist velocity at the expense of a lower maximum observable altitude. At tropical latitudes, EC-CPR had been operated with the 20-km mode until it was switched to the 18-km mode on 8 July 2025 (Imura et al., 2026). The corresponding Nyquist veolocity is about $5\,\mathrm{m\,s^{-1}}$ (Illingworth et al., 2015; Hagihara et al., 2023). Doppler measurements could exceed this value in cases like falling raindrops and intense updraft in extreme convection. It is very difficult in the latter case to unfold the aliased w_D profiles.

Multiple scattering (MS) occurs when a weather radar, especially a high-frequency radar like EC-CPR, observes thick, heavily precipitating clouds such as deep convective towers. MS makes a transmitted echo travel over extra distance before returning to the receiver, causing an effect known as pulse stretching. A notable stretching effect detected by a downlooking radar can lead to a long tail of echo extending to far below the surface, which is often called the MS tail (Battaglia and Simmer, 2008). A MS tail is recorded in EC-CPR observations as a second-trip echo, or a ghost echo emerging at a high altitude in the subsequent scan. Second-trip echoes arise also from mirror images, or the bogus echoes resulting from the radar pulses reflected back and forth between clouds and surface. Upper-tropospheric cloud cover estimated from EC-CPR could be falsely enhanced by a few percents due to mirror image echoes and to a much lesser extent by MS tails (Battaglia, 2021).

It is attempted to detect Doppler velocity folding in rainfall, MS tails, and mirror image echoes in the L1 data processing (Nakajima et al., 2026). Corrections to these artifacts are applied to the downstream L2 products. Doppler velocity folding is not expected in any case to impose considerable impacts on anvil clouds, in which neither vertical air motion nor sedimentation speed likely exceeds the Nyquist velocity of $\sim 5\,\mathrm{m\,s^{-1}}$. MS tails are unlikely either for moderate and small cloud optical depths as typical of cirrus anvils. On the other hand, it was found at an early stage of the analysis that mirror image echoes were partially left unfiltered in the L2 Doppler data. These remaining mirror images are removed in a simple method described in Appendix A.

https://doi.org/10.5194/egusphere-2026-3173
Preprint. Discussion started: 11 June 2026

Doppler velocity is contaminated with the satellite motion if CPR's line of sight (LOS) deviates away from nadir. The LOS contamination has been corrected in JAXA's EarthCARE L2 products with the exception of antenna mispointing errors originating from a thermal distortion of the antenna structure. Thermal distortions are considered to occur periodically over the orbital cycle, since the antenna would experience the largest thermal stress as the satellite flies over near the poles from the sunlit side of the planet to the other and vice versa. This is confirmed by the data indicating that the effects of antenna mispointing on Doppler measurements of ice clouds are gravest at polar latitudes while small at low latitudes (Puigdomènech Treserras et al., 2025) . No attempt is made in this study, targeted exclusively on tropical clouds, to apply antenna mispointing corrections.

3 In-cloud vertical motion

The in-cloud vertical motion estimates from EarthCARE are shown in this section, first on a snapshot-by-snapshot basis (Section 3.1) and then with composite statistics (Sections 3.2 and 3.3).

3.1 Example snapshots

Five events of organized convective systems are chosen from different regions over tropical oceans in Fig. 1, where each row shows the same snapshot but for different variables and products. The selected events vary from one to another in structural detail but have in common that a thick cloud layer penetrating from below the freezing level (~5 km) to the upper troposphere is accompanied by anvil cloud. The left two columns show that IWC, nearly as large as $1\,\mathrm{g\,m^{-3}}$ deep inside convective towers, tends to decrease with increasing height. IWC may remain relatively large in anvil clouds in some cases (e.g., the top row) but can be smaller than $10^{-2}\,\mathrm{g\,m^{-3}}$ in others (e.g., the bottom row). The CPR-ATLID IWC overall agrees with the CPR-only IWC except near cloud top, where the CPR-ATLID product captures the edges of clouds with a very small IWC (colored in light yellow) that are undetected by CPR alone. This is as expected owing to the greater sensitivity of ATLID to cloud ice compared to CPR.

Vertical air velocity is plotted in the right two columns of Fig. 1. A striking updraft is found in penetrating cloud layers, e.g., from $-2°$ to $0°$ latitude in the first example, around $6°$ in the third, and at $10°$ in the fourth, whereas anvil clouds have a relatively modest vertical motion as anticipated. The vertical motion profiles seemingly exhibit little apparent difference between the two products. A closer examination, however, reveals that $w_{a,c}$ is slightly but systematically larger in the CPR-ATLID than in the CPR, as most noticeable in the second example.

3.2 Doppler velocity versus air motion

The observed statistics of ice clouds are next examined in terms of IWP. IWP, or the column-integrated mass of cloud ice, may be viewed as a simple metric to conveniently separate deep convective cores (IWP $> 10^3\,\mathrm{g\,m^{-2}}$) from anvil clouds (10 g m^{-2} $<$ IWP $< 10^3\,\mathrm{g\,m^{-2}}$) and thin cirrus (IWP $< 10\,\mathrm{g\,m^{-2}}$), following the definition of Sokol and Hartmann (2020).

The histogram of IWP from the CPR-only and CPR-ATLID products is shown in Fig. 2. The two products yield qualitatively similar histograms, but a discrepancy is manifest. The CPR-only histogram is skewed toward larger IWPs in comparison with

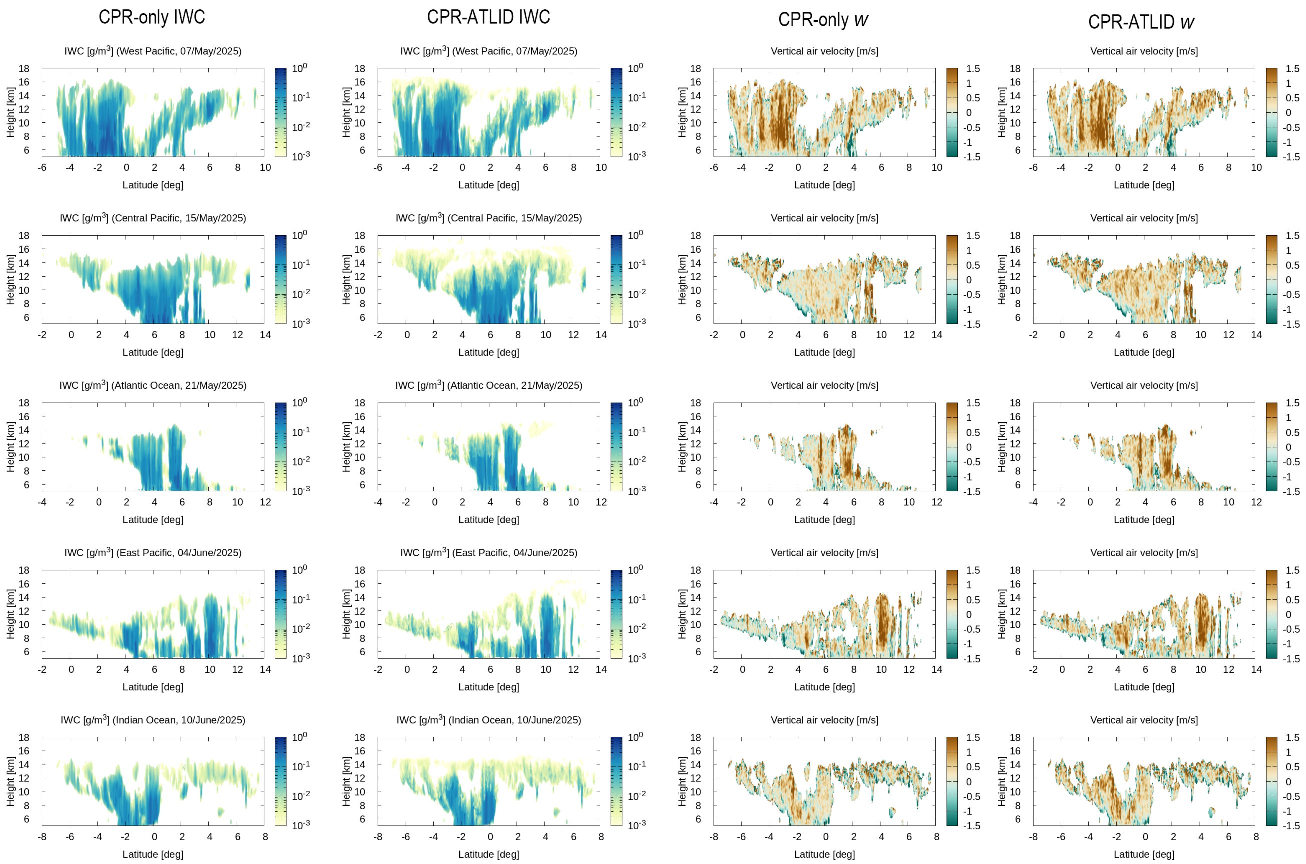

Figure 1. Five selected snapshots in longitude-height cross sections of IWC ($\mathrm{g\,m^{-3}}$, left two columns) and in-cloud vertical air velocity $w_{a,c}$ ($\mathrm{m\,s^{-1}}$, right two columns) for altitudes above 5 km. The EarthCARE radar-only (2A.CPR_CLP) product is compared with the radar-lidar (2B.AC_CLP) synergy product for each variable. The region and date of observation are indicated above each panel.

the CPR-ATLID statistics, suggesting that IWP in the CPR-only product may tend to be overestimated relative to the CPR-ATLID estimates. An overestimation of IWP in theory implies that, all else being equal, cloud particles are assumed to be too small, because ice water mass is inversely correlated with particle size under a fixed radar reflectivity. This indeed turns out to be the case as will be shown later in Section 3.3. The lidar's excellent detectability of semi-transparent clouds may partly explain the difference as well toward the lower end of the histogram.

Figure 3 presents cloud fraction, w_D, w_t, and $w_{a,c}$ averaged into a composite IWP-height diagram, as done in some past work (Ohno and Satoh, 2018; Gasparini et al., 2019). It is noted that IWPs smaller than $1\,\mathrm{g\,m^{-2}}$, although not negligible in occurrence as seen in Fig. 2 above, are set outside the range in order to narrow the focus on anvil clouds and convective cores. The CPR-only product is adopted to plot Fig. 3.

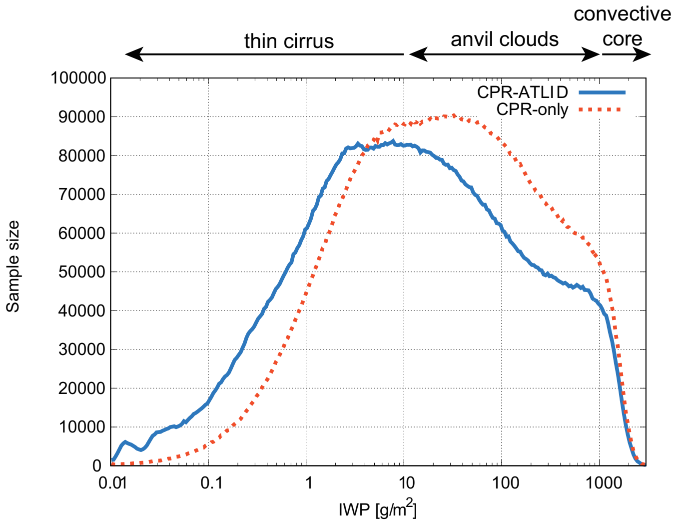

Figure 2. Histogram of IWP from the CPR-only (dotted) and CPR-ATLID (solid) products, defined by logarithmically uniform bins with the width of 0.02. Three cloud types of convective cores, anvil clouds, and thin cirrus labeled at the top are as defined by Sokol and Hartmann (2020).

Cloud fraction in IWP-height space (Fig. 3a) offers a clear statistical representation of deep convection at the largest IWPs and anvil clouds gradually thinning as they extend toward smaller IWPs (c.f., Fig. 1 of Gasparini et al., 2019). Doppler velocity (Fig. 3b) is found to be negative (downward) almost throughout the whole domain, most notably for large IWPs just above the freezing level of $\sim 5\,\mathrm{km}$. Terminal velocity (w_t) notably increases toward the lower-right corner of the plote (Fig. 3c), where precipitating ice is expected to be abundant and grown in size (Section 3.3). Doppler velocity is nearly zero above $12\,\mathrm{km}$ in height for an intermediate range of IWP.

In-cloud vertical air velocity implies an intense updraft inside convective cores and a modest ascent in anvil clouds (Fig. 3d). This overall structure of composite $w_{a,c}$ meets intuitive expectations and bears qualitative resemblance to simulated IWP-height diagrams from past numerical studies (Ohno and Satoh, 2018; Gasparini et al., 2022). Surprising, though, is the striking contrast between Fig. 3b and Fig. 3d, that is, $w_{a,c}$ and w_D exhibit remarkably different patterns despite the fact that the former is derived from the latter. This discrepancy may be understood through a careful inspection of w_t. For example, one can see from the contoured diagrams that terminal velocity monotonically enhances with IWP along any given height (Fig. 3c), whereas Doppler velocity no longer increases with IWP or even turns to diminish at the same altitude once IWP exceeds $10^3\,\mathrm{g\,m^{-2}}$ (Fig. 3b). The resulting combination of a largely negative w_t and a modestly negative w_D for largest IWPs (i.e., convective cores) is attributed to an intense in-cloud updraft (a large positive $w_{a,c}$) according to Eq. (1).

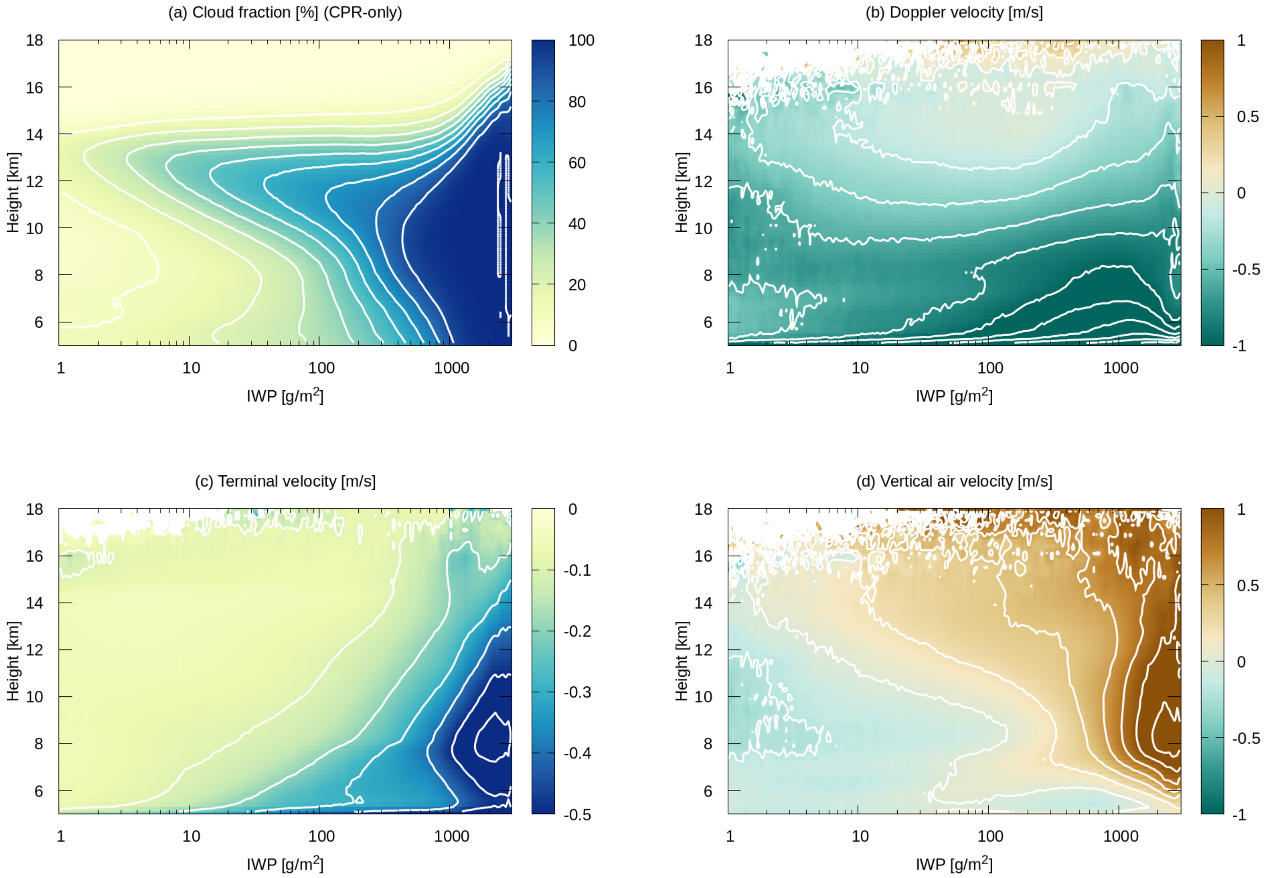

Figure 3. Composite IWP-height diagrams of (a) cloud fraction (%), (b) Doppler velocity w_D ($\mathrm{m\,s^{-1}}$), (c) Terminal velocity w_t ($\mathrm{m\,s^{-1}}$), and (d) In-cloud vertical air velocity $w_{a,c}$ ($\mathrm{m\,s^{-1}}$). The contour intervals are 10 % in (a), 0.2 $\mathrm{m\,s^{-1}}$ in (b) and (d), 0.1 $\mathrm{m\,s^{-1}}$ in (c). Velocity is defined as upward positive. All the plots are based on the CPR-only product (2A.CPR_CLP).

3.3 CPR-only versus CPR-ATLID retrievals

It was shown in Fig. 3 that convective cores and anvil clouds are observed with positive $w_{a,c}$ even where w_D is negative. This disparity between $w_{a,c}$ and w_D is explained by the disproportionately large size-dependence of $w_{t,Z}$. Doppler velocity could be negative when even only a handful of hydrometeors are large enough to fall out while the remaining majority stays within the ascending air. It follows that an adequate characterization of PSD is crucial for evaluating $w_{a,c}$ from Doppler measurements. Although the Doppler capability is equipped only with CPR, ATLID yields a useful constraint on the determination of PSD when combined with CPR (Okamoto et al., 2003). It is thus a simplistic but useful exercise to compare the CPR-only and CPR-ATLID products for grasping to what extent an inconsistency in PSD could impact on the estimation of $w_{a,c}$.

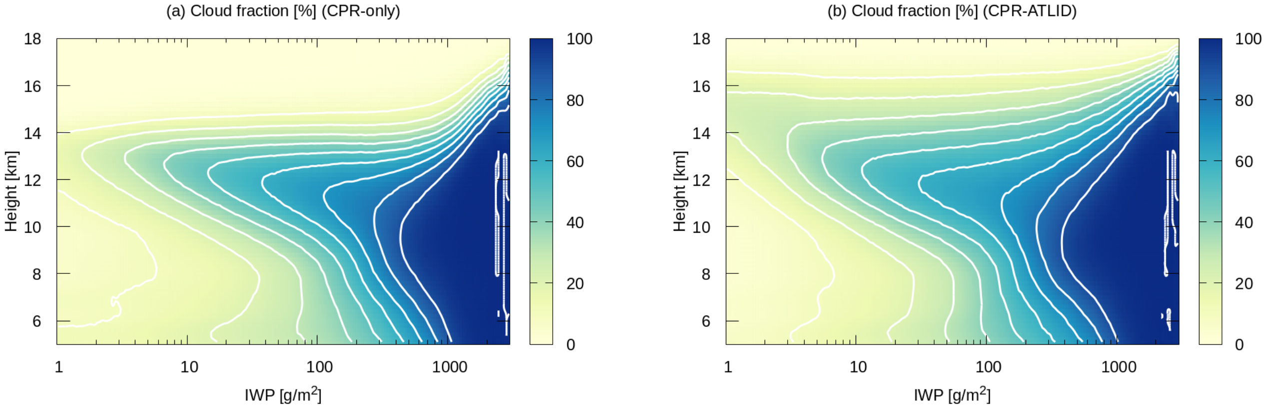

Figure 4. Composite IWP-height diagrams of (a) CPR-only cloud fraction (%) as Fig. 3a and (b) CPR-ATLID cloud fraction (%). The contour interval is 10 %.

The CPR-only cloud fraction is contrasted with its CPR-ATLID counterpart in Fig. 4a-b. While the overall cloud structure is shared in common, CPR-ATLID captures a greater amount of clouds at high altitudes beyond 14 km than CPR alone, as already confirmed in selected snapshots (Fig. 1). Otherwise any discernible difference is absent in cloud fraction, since lidar signals are rapidly lost by attenuation as they travel deeper in the cloud layer.

The impact of lidar measurements on cloud microphysics can be more far-reaching. The cloud PSD has control over the extinction of radar and lidar echoes as well as their back-scattering efficiency. Any difference in PSD parameters hence not only locally influences the retrieval but also in the layer immediately below through attenuation correction. A consecutive chain of this effect could eventually reach all levels beneath, leading to the propagation of cloud-top information throughout the cloud.

The 2A.CPR_CLP and 2B.AC_CLP products contain mode-1 and mode-2 cloud effective radii, denoted hereafter by $r_{e,1}$ and $r_{e,2}$, corresponding to precipitating and non-precipitating particles, respectively. Figure 5 compares $r_{e,1}$ and $r_{e,2}$ from the two products in IWP-height space. A sharp increase toward the lower-right corner in the composite pattern of $r_{e,1}$ is shared by the two products (Fig. 5a, c). To the contrary, the CPR-only and CPR-ATLID estimates of $r_{e,2}$ strikingly disagree with each other. In the CPR-only product, $r_{e,2}$ is nearly homogeneous below 10 km in altitude and entirely missing above (Fig. 5b), while $r_{e,2}$ is highly variable throughout the domain up to 14 km or even higher in the CPR-ATLID product (Fig. 5d). The rich variability in the latter is as expected because ATLID is able to detect small (mode-2) particles that may be missed to a large degree by CPR.

The mode-2 cloud particles are so small that the *direct* impact of the second mode on w_t, and thereby on $w_{a,c}$, is secondary. The first mode almost exclusively accounts for w_t, as visually evident from a structural resemblance of $r_{e,1}$ (Fig. 5a,c) to w_t (Fig. 3c). The second mode, nonetheless, is by no means negligible in that the mode-1 PSD is forcibly skewed in compensation for the discrepancies in $r_{e,2}$ under the constraint of a given observations. As color-shaded in Fig. 6a, the mode-1 effective radius

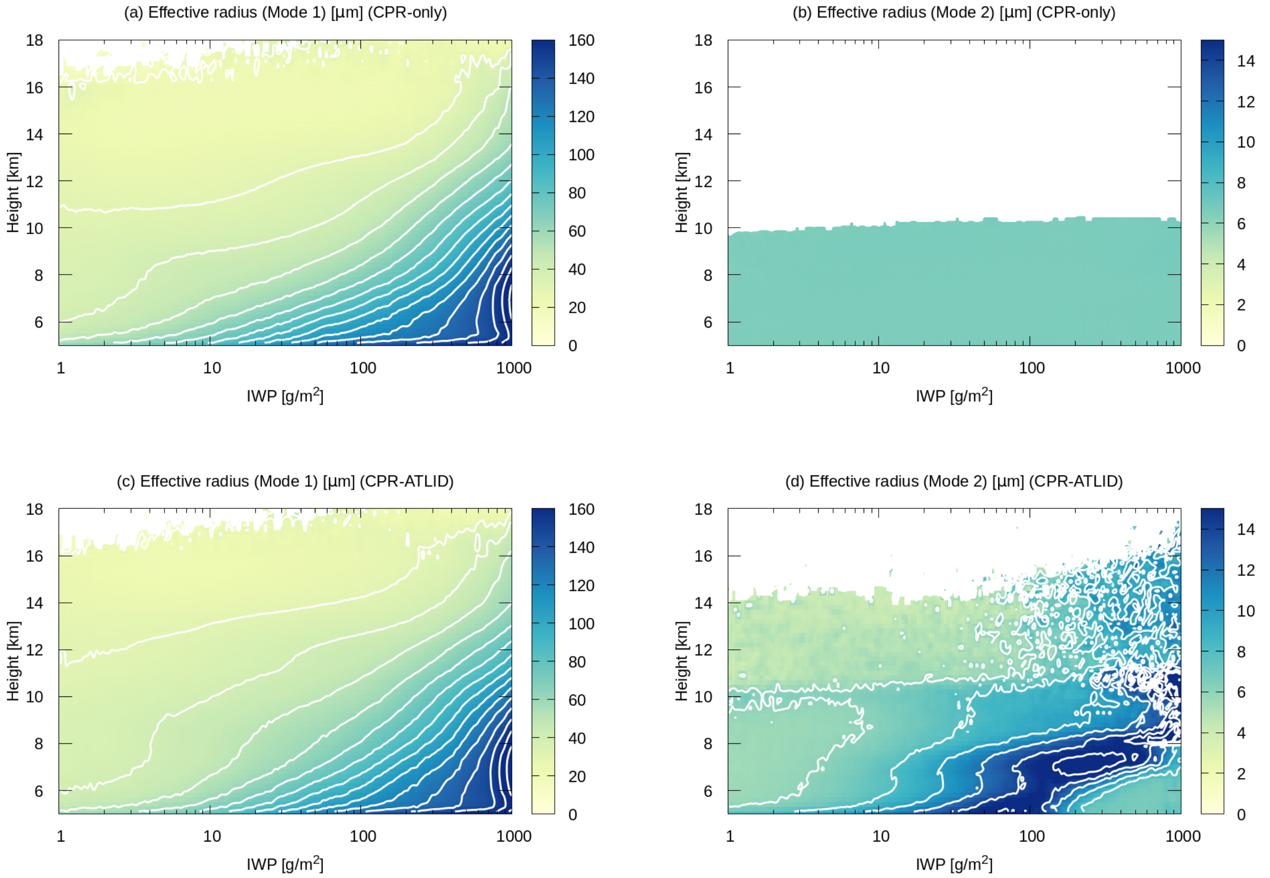

Figure 5. Composite IWP-height diagrams of (a) $r_{e,1}$ from CPR-only, (b) $r_{e,2}$ from CPR-only, (c) $r_{e,1}$ from CPR-ATLID, and (c) $r_{e,2}$ from CPR-ATLID. The contour interval is 10 μm for (a) and (c) and is 2 μm for (b) and (d). The range of variability is so narrow that contours are not visible in (b).

tends to be consistently smaller in the CPR-only product than in the CPR-ATLID, except in the close vicinity of the freezing level where the bias switches in sign. A negative bias in effective radius leads to a smaller fall speed, and hence results in an overall underestimation of the CPR-only $w_{a,c}$ relative to the CPR-ATLID as can be confirmed in Fig. 6b. The inter-product bias in $w_{a,c}$ nevertheless remains modest in magnitude (within $\pm 0.2\,\mathrm{m\,s^{-1}}$). The CPR-only $w_{a,c}$ (Fig. 3d) visually compares well to the CPR-ATLID counterpart as contoured in Fig. 6b, assuring that the overall pattern of $w_{a,c}$ is qualitatively robust.

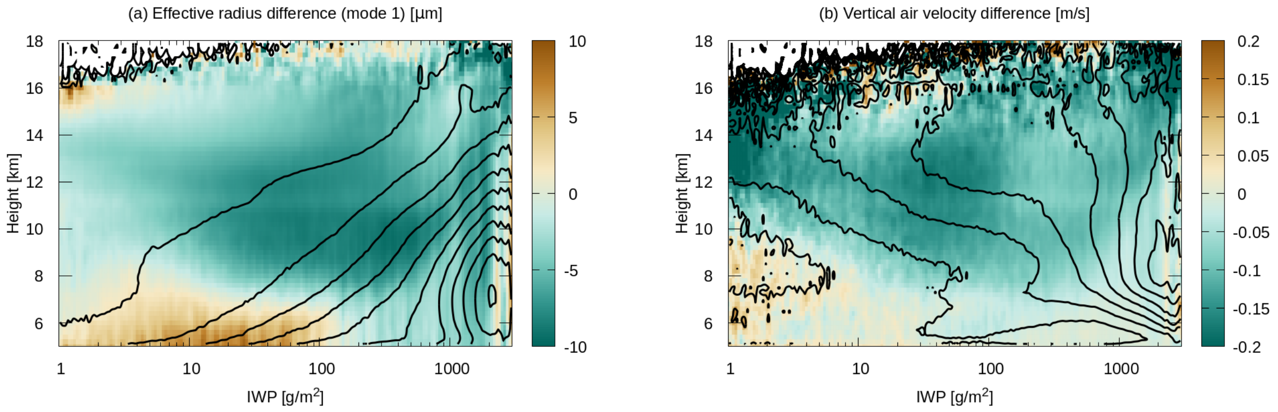

Figure 6. Composite IWP-height diagrams of (a) The mode-1 particle effective radius from CPR-ATLID (μm, contoured) and its inter-product difference (CPR-only − CPR-ATLID, in color) and (b) In-cloud vertical air velocity from CPR-ATLID ($\mathrm{m\,s^{-1}}$, contoured) and its inter-product difference (CPR-only − CPR-ATLID, in color). The contour intervals are 20 μm in (a) and $0.2\,\mathrm{m\,s^{-1}}$ in (b).

4 Circulation field in anvil clouds

The composite diagrams shown in the previous section illustrate the mean vertical profiles sorted by IWP instead of a spatial dimension. Although the observed structure of anvil clouds and convective cores in 4a-b is reminiscent of an organized convective system as we know it, adjacent columns in IWP space are not guaranteed to represent physical neighbors. In this section, similar composite plots are constructed but this time sorted by horizontal distance in place of IWP. The distance-height diagram of vertical air velocity enables to delineate a two-dimensional picture of horizontal wind and thus of circulation field.

4.1 Method

The current approach is conceptually similar to previous methods based on radar-detected cloud features (Igel et al., 2014; Ito and Masunaga, 2022) or infrared-measured cloud properties (Protopapadaki et al., 2017; Sokol and Hartmann, 2020) but differs in that convective cores and anvils are separated simply by IWP. A convective core is defined as a series of consecutive cloudy columns that each satisfy the empirical definition of IWP $> 10^3\,\mathrm{g\,m^{-2}}$ over a distance of $\pm R_c$. The convective core radius, R_c, is known to span a broad range with the median of about 5 km over tropical oceans (Takahashi et al., 2023). All convective cores with $R_c \geq 1\,\mathrm{km}$ are included in the present analysis to secure a sufficient sample size. A more restrictive definition of $R_c \geq 5\,\mathrm{km}$ was also tested and confirmed not to qualitatively alter the results.

An along-track sequence of observed columns is sampled around each convective core. This procedure is repeated with all qualifying convective cores over the study region and period (Section 2.1). The resulting collection of column sequences are averaged into a composite diagram as a function of horizontal distance measured from the core center, with the caveat that any column with IWP $> 10^3\,\mathrm{g\,m^{-2}}$ outside $\pm R_c$ is excluded from the averaging. This caveat is intended to ensure that composite anvil clouds are not contaminated by neighboring convective cores that exist often, as clearly visible in Fig. 1.

The mass conservation law in the axisymmetric cylindrical coordinates yields radial wind, u_r, as

$$\frac{1}{r}\frac{\partial}{\partial r} r u_r(r,z) = D(r,z), \tag{2}$$

where D designates horizontal divergence,

$$D(r,z) = -\frac{\partial w_a(r,z)}{\partial z}. \tag{3}$$

Here all-sky vertical velocity, w_a, is defined with a combination of $w_{a,c}$ and ambient (clear-sky) vertical velocity, $w_{a,a}$, as

$$w_a(r,z) = f_c(r,z) w_{a,c}(r,z) + [1 - f_c(r,z)] w_{a,a}(r,z). \tag{4}$$

Cloud fraction, f_c, and $w_{a,c}$ are as estimated from EarthCARE observations, while $w_{a,a}$ is prescribed as explained later. The solution $u_r(r,z)$ is obtained by integrating Eq. (2) over r from $r=0$ at each level with the symmetry-required boundary condition of $u_r(0,z)=0$. The distribution of wind vectors $(u_r,\, w_a)$ in r-z space depicts a circulation field representing the anvil cloud dynamics.

The axisymmetric assumption is valid for isotropic anvil outflows from a point-source-like convective core as may occur in the absence of appreciable background wind. Axisymmetry, however, would not fit highly anisotropic convective systems like squall lines, with anvil clouds expanding nearly perpendicularly to a line of convective clouds. In such cases, the Cartesian continuity equation may offer a more appropriate approximation,

$$\frac{\partial u_x(x,z)}{\partial x} = D(x,z), \tag{5}$$

where u_x is Cartesian horizontal wind. Equations (3) and (4) remain unchanged in the Cartesian coordinates except that r is to be replaced by x.

The only input variable unavailable from EarthCARE is $w_{a,a}$, as EC-CPR is by design unable to detect anything outside clouds. The possible origins of $w_{a,a}$ range from radiatively-driven clear-sky subsidence to dynamically-forced ascent and descent such as gravity waves (Poujol and Bony, 2024). In this preliminary analysis, such complex variability of clear-sky vertical air motion is not considered but instead $w_{a,a}$ is simply assumed to be absent everywhere, that is,

$$w_a(r,z) \approx f_c(r,z) w_{a,c}(r,z). \tag{6}$$

This is a workable (though not always realistic) assumption to the extent that $w_{a,a}$ changes more smoothly over height than $w_{a,c}$, with the fact in mind that w_a affects horizontal wind only through its vertical gradient.

4.2 Result

Figure 7a shows composite cloud fraction in the distance-height plane. Anvil clouds are clearly visible as a layer of enhanced cloudiness peaked around a height of 12 km. Intense updraft trapped within the convective core on the left end of the plot gives

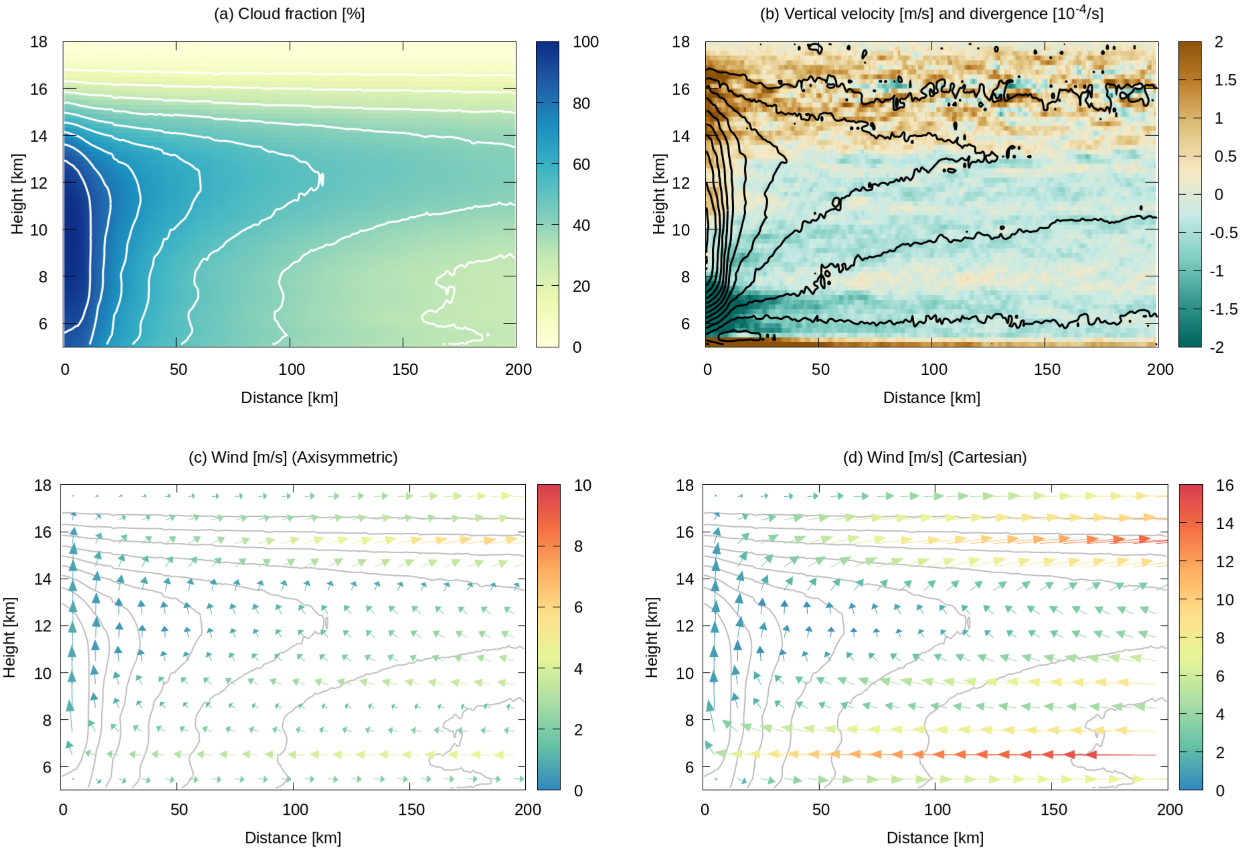

Figure 7. Composite distance-height diagrams of (a) Cloud fraction (%), (b) Vertical air velocity w_a ($\mathrm{m\,s^{-1}}$, contoured) and horizontal divergence D ($10^{-4}\,\mathrm{s^{-1}}$, in color), (c) Axisymmetric horizontal-vertical wind field with the amplitude color scaled ($\mathrm{m\,s^{-1}}$), overlaid by contoured cloud fraction, and (d) As (c) but for Cartesian winds. The contour intervals are 10 % in (a), (c)-(d), and 0.1 $\mathrm{m\,s^{-1}}$ in (b). The horizontal axis is defined as the along-track distance from deep convective cores (see text for details). All the plots are constructed with the CPR-ATLID product.

way to modest ascent in w_a (contours in Fig. 7b). The w_a contours at a distance of, say, 100 km implies an upward acceleration until w_a reaches a maximum at $\sim$13 km in altitude and sharply declines beyond. The contrasting pair of acceleration and deceleration generates a layer of horizontal convergence topped by a diverging TTL as color-shaded in Fig. 7b.

The derived u_r and w_a together delineates a well-defined trajectories of vector fields comprised of a mid-level inflow below about 13 km and an upper-level outflow above (Fig. 7c), reminiscent of the mid- to upper-tropospheric circulation archetypical of mesoscale convective dynamics (Moncrieff, 1992; Kingsmill and Houze Jr., 1999). A similar circulation pattern was found also in numerical simulations of anvil clouds formed in association with isolated convection (Gasparini et al., 2019).

https://doi.org/10.5194/egusphere-2026-3173
Preprint. Discussion started: 11 June 2026

The Cartesian circulation is qualitatively identical to the axisymmetric winds (Fig. 7d). Wind speed, however, is estimated to be larger in the Cartesian geometry. The overestimation is most conspicuous at the farthest end away from the core, since axisymmetric (ring-shaped) horizontal divergence is geometrically diluted with increasing radius while Cartesian divergence is independent of distance. Figures 7c-d show that the upper-tropospheric outflow keeps accelerating over distance regardless of geometry, which is an implausible outcome largely due to the assumption that ambient vertical motion is absent. The unlikely acceleration of horizontal wind driven so far away from convective updraft would be rectified when realistic clear-sky subsidence is taken into account to avoid falsely large upper-tropospheric divergence.

The mesoscale circulation depicted in Figure 7 is more of an observational confirmation of the anvil cloud dynamics as known in the literature than a new addition to the current state of understanding. The result is nevertheless encouraging for future studies in that the EarthCARE products are proven not only to provide reliable measurements of in-cloud vertical air motion but to be able to offer two-dimensional wind vector as well.

5 Conclusions

Early observations from EarthCARE over global tropical oceans are investigated in this work to assess the potential of Doppler measurements from space for exploring the dynamics of tropical anvil clouds. Two of JAXA's cloud products derived with EC-CPR only (2A.CPR_CLP) and CPR and ATLID in tandem (2B.AC_CLP) are analyzed with focus on the IWP-sorted vertical structure of in-cloud vertical air velocity. Vertical air velocity derived from CPR Doppler measurements implies an intense updraft within convective cores and a modest ascent in anvil clouds. This result, although as intuitively expected, is not self-evident given the fact that Doppler velocity itself is predominantly negative (downward) or near zero throughout the IWP-height plane.

The Doppler estimation of sedimentation (terminal) velocity, and consequently of in-cloud vertical air velocity, relies sensitively on the microphysical model assumed in the retrieval algorithm. An extra observational constraint by ATLID on the PSD model updates the estimation of vertical air velocity in the ATLID-CPR product. Although the in-cloud domain where CPR and ATLID observations are available at the same time is limited to a narrow layer near cloud top, the benefit of simultaneous measurements by the two sensors extends to the whole ice-cloud layer. The effective radius of precipitating ice is consistently larger in the CPR-ATLID product than in the CPR-only, while the overall pattern of in-cloud vertical velocity is largely shared by the two products.

EC-CPR is a nadir-looking radar with its Doppler capability designed exclusively to measure vertical motion. It is nonetheless demonstrated in this work that diagnostic horizontal wind may be derived as well so that mass conservation is satisfied. The velocity vector field manifests itself as a familiar mesoscale circulation constituted of a mid-tropospheric inflow toward the convective core below a height of about 13 km and an upper-tropospheric outflow above. This result, although based on simplified assumptions to be refined in future work, underscores EarthCARE's technological utility for studying the dynamics of anvil clouds.

The current assumptions for the calculation of horizontal wind include idealized (axial or Cartesian) symmetry and zero vertical motion in the ambient air. The latter, in particular, is obviously oversimplified and to be improved in future work. The fundamental challenge is that existing satellite missions lack any instrument to observe vertical air motion outside clouds. As a notable exception, Poujol and Bony (2024) developed a novel methodology to derive mid-tropospheric clear-sky vertical velocity from temporal variations in geostationary vapor-channel brightness temperature. This product, once made available for the EarthCARE mission period, would offer a useful observational input as a realistic estimate of $w_{a,a}$.

As a next step, the present analysis will be extended to include JAXA's EarthCARE radiation product (2B.ALL_RAD) as the ongoing reprocessing of this product is completed over an extended period back in time. The 2B.ALL_RAD product provides the vertical profiles of radiative flux that is physically consistent with the cloud properties from 2B.AC_CLP. A follow-up study being planned will shed light on the radiatively driven dynamics of anvil clouds based on a joint analysis of radiative heating and Doppler-derived circulation field.

Appendix A: Removal of mirror image echoes

Distinctly large values of w_D were originally found at altitudes higher than 16 km in the composite IWP-height space (Fig. A1a). These anomalous values are associated with weak radar signals corresponding to small IWCs below $10^{-2}\,\mathrm{g\,m^{-3}}$, giving rise to a "wing" outside the vertical histogram ridge where a vast majority of samples reside (Fig. A1c). The histogram ridge, confined to modest values of w_D within $\pm 1\,\mathrm{m\,s^{-1}}$, is likely attributed to TTL cirrus, whereas the wing is presumably second-trip echoes due to mirror images (see Section 2.2). A Doppler velocity of a few $\mathrm{m\,s^{-1}}$ is too large for TTL cirrus but instead may be reasonably interpreted as a mirror image arising from falling raindrops. The fact that this artifact avoids extremely large IWPs beyond $10^3\,\mathrm{g\,m^2}$ (Fig. A1a) suggests that these second-trip echoes are more likely mirror images than MS tails. Although the JAXA EarthCARE data processing attempts to isolate out mirror image echoes, a certain fraction of them apparently remain undetected.

In this work, any samples above 16 km in altitude are retained only when $w_D < 1\ \mathrm{m\,s^{-1}}$ and otherwise excluded from the analysis to remove the remaining mirror image echoes. Figure A1b shows the same plot as Fig. A1a but after the correction applied. The mirror images are largely, if not completely, removed from w_D by the correction.

Data availability.

The 2A.CPR_CLP (https://doi.org/10.57746/EO.01jdvd2gqq34e6yz9p8kfe68x5) and 2B.AC_CLP (https://doi.org/10.57746/EO.01jkwjeg2y0bqndnsvjvaaskaw) datasets are freely available through JAXA G-Portal (https://gportal.jaxa.jp/gpr/).

Author contributions.

HM is responsible for all aspects of this research including concept design, data analysis, and writing the paper.

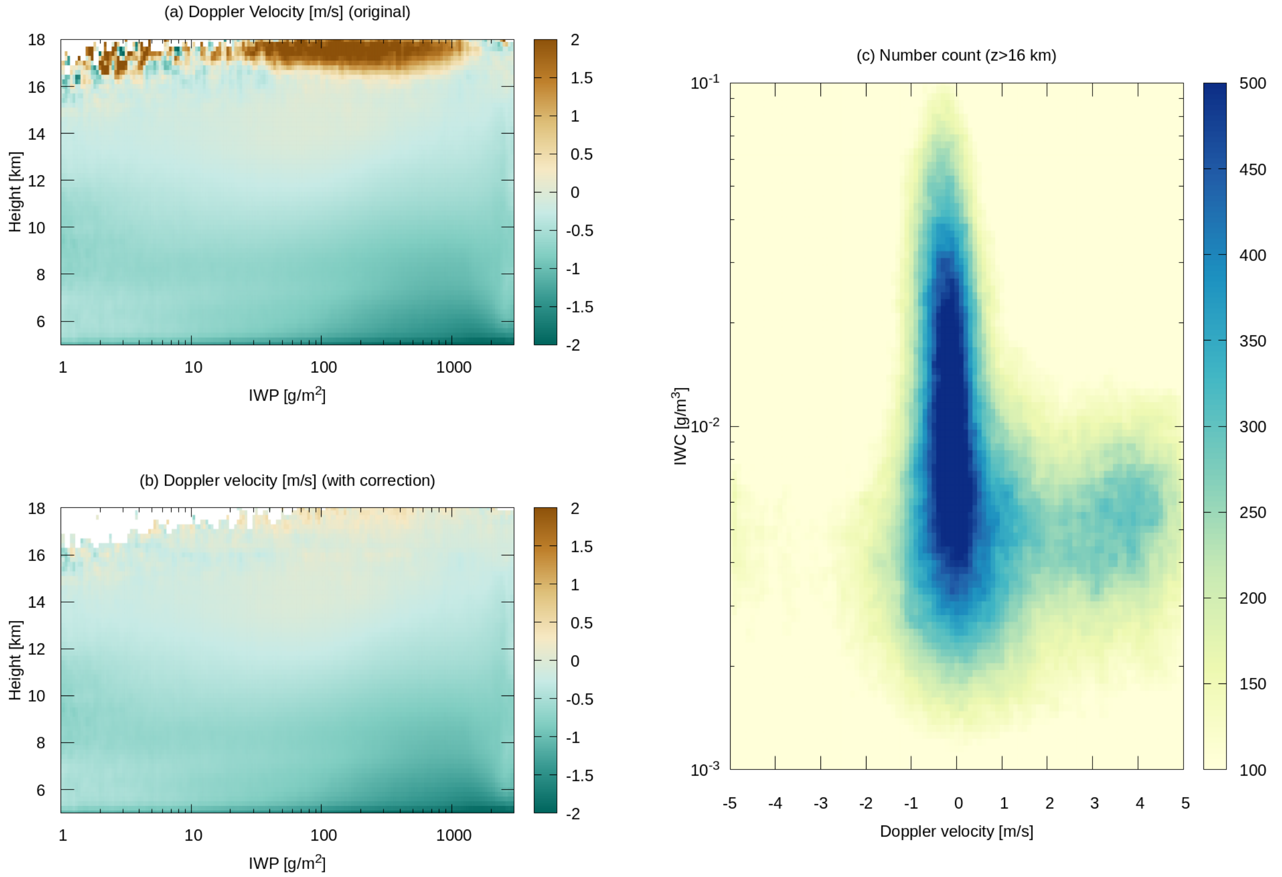

Figure A1. (a) Uncorrected Doppler velocity composited in the IWP-altitude plane. (b) As (a) with mirror image echoes removed. (c) Two-dimensional histogram of the upper-tropospheric ($z > 16$ km) samples as a function of Doppler velocity and IWC.

Competing interests.

The author has no competing interests to disclose.

Acknowledgements. The efforts of the JAXA/ESA EarthCARE science teams for the successful mission operation and dataset production are greatly appreciated. The EarthCARE datasets analyzed in this work, 2A.CPR_CLP and 2B,AC_CLP, were provided by JAXA. The author thanks Shunsuke Aoki for his comments on EC-CPR second-trip echoes discussed in Appendix A. This work is supported by Japan Society for the Promotion of Science (JSPS) Grants-in-Aid for Scientific Research (KAKENHI) Grant Number 25K07398.

References

Ackerman, T. P., Liou, K.-N., Valero, F. P. J., and Pfister, L.: Heating Rates in Tropical Anvils, J. Atmos. Sci., 45, 1606–1623, https://doi.org/10.1175/1520-0469(1988)045<1606:HRITA>2.0.CO;2, 1988.

Aoki, S., Kubota, T., and Turk, F. J.: Exploring vertical motions in convective and stratiform precipitation using spaceborne radar observations: insights from EarthCARE and GPM coincidence dataset, Atmos. Meas. Tech., 19, 79–100, https://doi.org/10.5194/amt-19-79-2026, 2026.

Battaglia, A.: Impact of second-trip echoes for space-borne high-pulse-repetition-frequency nadir-looking W-band cloud radars, Atmos. Meas. Tech., 14, 7809–7820, https://doi.org/10.5194/amt-14-7809-2021, 2021.

Battaglia, A. and Simmer, C.: How Does Multiple Scattering Affect the Spaceborne W-Band Radar Measurements at Ranges Close to and Crossing the Sea-Surface Range?, IEEE Trans. Geosci. Remote Sens., 46, 1644–1651, https://doi.org/10.1109/TGRS.2008.916085, 2008.

Bony, S., Stevens, B., Coppin, D., Becker, T., Reed, K. A., Voigt, A., and Medeiros, B.: Thermodynamic control of anvil cloud amount, Proc. Natl. Acad. Sci. USA, 113, 8927–8932, https://doi.org/10.1073/pnas.1601472113, 2016.

Deng, M. and Mace, G. G.: Cirrus Microphysical Properties and Air Motion Statistics Using Cloud Radar Doppler Moments. Part I: Algorithm Description, J. Appl. Meteor. Climatol., 45, 1690–1709, https://doi.org/10.1175/JAM2433.1, 2006.

Eisinger, M., Marnas, F., Wallace, K., Kubota, T., Tomiyama, N., Ohno, Y., Tanaka, T., Tomita, E., Wehr, T., and Bernaerts, D.: The EarthCARE mission: science data processing chain overview, Atmos. Meas. Tech., 17, 839–862, https://doi.org/10.5194/amt-17-839-2024, 2024.

Fueglistaler, S., Dessler, A. E., Dunkerton, T. J., Folkins, I., Fu, Q., and Mote, P. W.: Tropical tropopause layer, Rev. Geophys., 47, RG1004, https://doi.org/10.1029/2008RG000267, 2009.

Galfione, A., Battaglia, A., Puigdomènech Treserras, B., and Kollias, P.: First insights into deep convection by the Doppler velocity measurements of the EarthCARE Cloud Profiling Radar, Atmos. Meas. Tech., 18, 6747–6763, https://doi.org/10.5194/amt-18-6747-2025, 2025.

Garrett, T. J., Navarro, B. C., Twohy, C. H., Jensen, E. J., Baumgardner, D. G., Bui, P. T., Gerber, H., Herman, R. L., Heymsfield, A. J., Lawson, P., Minnis, P., Nguyen, L., Poellot, M., Pope, S. K., Valero, F. P. J., and Weinstock, E. M.: Evolution of a Florida Cirrus Anvil, J. Atmos. Sci., 62, 2352–2372, https://doi.org/10.1175/JAS3495.1, 2005.

Gasparini, B., Blossey, P. N., Hartmann, D. L., Lin, G., and Fan, J.: What Drives the Life Cycle of Tropical Anvil Clouds?, J. Adv. Model. Earth Syst., 11, 2586–2605, https://doi.org/10.1029/2019MS001736, 2019.

Gasparini, B., Sokol, A. B., Wall, C. J., Hartmann, D. L., and Blossey, P. N.: Diurnal Differences in Tropical Maritime Anvil Cloud Evolution, J. Climate, 35, 1655–1677, https://doi.org/10.1175/JCLI-D-21-0211.1, 2022.

Gasparini, B., Sullivan, S. C., Sokol, A. B., Kärcher, B., Jensen, E., and Hartmann, D. L.: Opinion: Tropical cirrus – from micro-scale processes to climate-scale impacts, Atmos. Chem. Phys., 23, 15 413–15 444, https://doi.org/10.5194/acp-23-15413-2023, 2023.

Hagihara, Y., Ohno, Y., Horie, H., Roh, W., Satoh, M., and Kubota, T.: Global evaluation of Doppler velocity errors of EarthCARE cloud-profiling radar using a global storm-resolving simulation, Atmos. Meas. Tech., 16, 3211–3219, https://doi.org/10.5194/amt-16-3211-2023, 2023.

Hartmann, D. L. and Larson, K.: An important constraint on tropical cloud-climate feedback, Geophys. Res. Lett., 29, https://doi.org/10.1029/2002GL015835, 2002.

Hartmann, D. L., Gasparini, B., Berry, S. E., and Blossey, P. N.: The Life Cycle and Net Radiative Effect of Tropical Anvil Clouds, J. Adv. Model. Earth Syst., 10, 3012–3029, https://doi.org/10.1029/2018MS001484, 2018.

Horner, G. and Gryspeerdt, E.: The evolution of deep convective systems and their associated cirrus outflows, Atmos. Chem. Phys., 23, 14 239–14 253, https://doi.org/10.5194/acp-23-14239-2023, 2023.

Hotta, H., Suzuki, K., Kikuchi, M., Aoki, S., and Kubota, T.: Characteristics of tropical clouds with strong updrafts revealed by Doppler velocity measurements from EarthCARE/CPR, EGUsphere, 2026, 1–34, https://doi.org/10.5194/egusphere-2026-659, 2026.

Igel, M. R., Drager, A. J., and van den Heever, S. C.: A CloudSat cloud object partitioning technique and assessment and integration of deep convective anvil sensitivities to sea surface temperature, J. Geophys. Res., 119, 10 515–10 535, https://doi.org/10.1002/2014JD021717, 2014.

Illingworth, A. J., Barker, H. W., Beljaars, A., Ceccaldi, M., Chepfer, H., Clerbaux, N., Cole, J., Delanoë, J., Domenech, C., Donovan, D. P., Fukuda, S., Hirakata, M., Hogan, R. J., Huenerbein, A., Kollias, P., Kubota, T., Nakajima, T., Nakajima, T. Y., Nishizawa, T., Ohno, Y., Okamoto, H., Oki, R., Sato, K., Satoh, M., Shephard, M. W., Velázzquez-Blázquez, A., Wandinger, U., Wehr, T., and van Zadelhoff, G.-J.: The EarthCARE Satellite: The Next Step Forward in Global Measurements of Clouds, Aerosols, Precipitation, and Radiation, Bull. Amer. Meteor. Soc., 96, 1311–1332, https://doi.org/10.1175/BAMS-D-12-00227.1, 2015.

Imura, Y., Aoki, S., Kubota, T., Nakatsuka, H., Ohno, Y., and Okamoto, H.: Observation modes of EarthCARE/CPR with different Doppler measurement accuracy: Evaluation of their applicability, EGUsphere, 2026, 1–27, https://doi.org/10.5194/egusphere-2026-1453, 2026.

Ito, M. and Masunaga, H.: Process-Level Assessment of the Iris Effect Over Tropical Oceans, Geophys. Res. Lett., 49, e2022GL097 997, https://doi.org/10.1029/2022GL097997, 2022.

Jensen, E. J., Toon, O. B., Pfister, L., and Selkirk, H. B.: Dehydration of the upper troposphere and lower stratosphere by subvisible cirrus clouds near the tropical tropopause, Geophys. Res. Lett., 23, 825–828, https://doi.org/10.1029/96GL00722, 1996.

Kärcher, B. and Spichtinger, P.: Cloud-controlling Factors of Cirrus, in: Clouds in the Perturbed Climate System: Their Relationship to Energy Balance, Atmospheric Dynamics, and Precipitation, edited by Heintzenberg, J. and Charlson, R. J., The MIT Press, https://doi.org/10.7551/mitpress/9780262012874.003.0011, 2009.

Kingsmill, D. E. and Houze Jr., R. A.: Kinematic characteristics of air flowing into and out of precipitating convection over the west Pacific warm pool: An airborne Doppler radar survey, Quart. J. Roy. Meteor. Soc., 125, 1165–1207, https://doi.org/10.1002/qj.1999.49712555605, 1999.

Kollias, P., Puidgomènech Treserras, B., Battaglia, A., Borque, P. C., and Tatarevic, A.: Processing reflectivity and Doppler velocity from EarthCARE's cloud-profiling radar: the C-FMR, C-CD and C-APC products, Atmos. Meas. Tech., 16, 1901–1914, https://doi.org/10.5194/amt-16-1901-2023, 2023.

Lilly, D. K.: Cirrus Outflow Dynamics, J. Atmos. Sci., 45, 1594–1605, https://doi.org/10.1175/1520-0469(1988)045<1594:COD>2.0.CO;2, 1988.

Luo, Z. and Rossow, W. B.: Characterizing tropical cirrus life cycle, evolution, and interaction with upper-tropospheric water vapor using Lagrangian trajectory analysis of satellite observations, J. Climate, 17, 4541–4563, 2004.

Mace, G. G., Heymsfield, A. J., and Poellot, M. R.: On retrieving the microphysical properties of cirrus clouds using the moments of the millimeter-wavelength Doppler spectrum, J. Geophys. Res., 107, AAC 22–1–AAC 22–26, https://doi.org/10.1029/2001JD001308, 2002.

Massie, S., Gettelman, A., Randel, W., and Baumgardner, D.: Distribution of tropical cirrus in relation to convection, J. Geophys. Res., 107, AAC 19–1–AAC 19–16, https://doi.org/10.1029/2001JD001293, 2002.

https://doi.org/10.5194/egusphere-2026-3173
Preprint. Discussion started: 11 June 2026

Masunaga, H.: The Edge Intensification of Eastern Pacific ITCZ Convection, J. Climate, 36, 3469–3480, https://doi.org/10.1175/JCLI-D-22-0382.1, 2023.

Masunaga, H. and Bony, S.: Radiative invigoration of tropical convection by preceding cirrus clouds, J. Atmos. Sci., 75, 1327–1342, https://doi.org/10.1002/2016MS000855, 2018.

Moncrieff, M. W.: Organized Convective Systems: Archetypal Dynamical Models, Mass and Momentum Flux Theory, and Parametrization, Quart. J. Roy. Meteor. Soc., 118, 819–850, https://doi.org/10.1002/qj.49711850703, 1992.

Muhlbauer, A., Kalesse, H., and Kollias, P.: Vertical velocities and turbulence in midlatitude anvil cirrus: A comparison between in situ aircraft measurements and ground-based Doppler cloud radar retrievals, Geophys. Res. Lett., 41, 7814–7821, https://doi.org/10.1002/2014GL062279, 2014.

Nakajima, T., Kikuchi, M., Ohno, Y., Horie, H., Okamoto, T., Nishizawa, T., Nakajima, T. Y., Suzuki, K., Satoh, M., and Kubota, T.: EarthCARE JAXA Level 2 Algorithm Theoretical Basis Document (L2 ATBD), https://www.eorc.jaxa.jp/EARTHCARE/document/reference/dev/EarthCARE_L2_ATBD.pdf, 2026.

Ohno, T. and Satoh, M.: Roles of Cloud Microphysics on Cloud Responses to Sea Surface Temperatures in Radiative-Convective Equilibrium Experiments Using a High-Resolution Global Nonhydrostatic Model, J. Adv. Model. Earth Syst., 10, 1970–1989, https://doi.org/10.1029/2018MS001386, 2018.

Ohno, T., Noda, A. T., Seiki, T., and Satoh, M.: Importance of Pressure Changes in High Cloud Area Feedback Due to Global Warming, Geophysical Research Letters, 48, e2021GL093 646, https://doi.org/10.1029/2021GL093646, 2021.

Okamoto, H., Iwasaki, S., Yasui, M., Horie, H., Kuroiwa, H., and Kumagai, H.: An algorithm for retrieval of cloud microphysics using 95-GHz cloud radar and lidar, J. Geophys. Res., 108, https://doi.org/10.1029/2001JD001225, 2003.

Orr, B. W. and Kropfli, R. A.: A Method for Estimating Particle Fall Velocities from Vertically Pointing Doppler Radar, J. Atmos. Oceanic Technol., 16, 29–37, https://doi.org/10.1175/1520-0426(1999)016<0029:AMFEPF>2.0.CO;2, 1999.

Poujol, B. and Bony, S.: Measuring Clear-Air Vertical Motions From Space, AGU Adv., 5, e2024AV001 267, https://doi.org/10.1029/2024AV001267, 2024.

Protat, A. and Williams, C. R.: The Accuracy of Radar Estimates of Ice Terminal Fall Speed from Vertically Pointing Doppler Radar Measurements, J. Appl. Meteor. Climatol., 50, 2120–2138, https://doi.org/10.1175/JAMC-D-10-05031.1, 2011.

Protopapadaki, S. E., Stubenrauch, C. J., and Feofilov, A. G.: Upper tropospheric cloud systems derived from IR sounders: properties of cirrus anvils in the tropics, Atmos. Chem. Phys., 17, 3845–3859, https://doi.org/10.5194/acp-17-3845-2017, 2017.

Puigdomènech Treserras, B., Kollias, P., Battaglia, A., Tanelli, S., and Nakatsuka, H.: EarthCARE's cloud profiling radar antenna pointing correction using surface Doppler measurements, Atmos. Meas. Tech., 18, 5607–5618, https://doi.org/10.5194/amt-18-5607-2025, 2025.

Roh, W., Satoh, M., Matsugishi, S., Aoki, S., Kubota, T., and Okamoto, H.: Vertical motions in clouds from EarthCare satellite and a global storm-resolving modeling, Sci. Rep., 16, 2622, https://doi.org/10.1038/s41598-025-32256-8, 2025.

Sato, K. and Okamoto, H.: Refinement of global ice microphysics using spaceborne active sensors, J. Geophys. Res., 116, https://doi.org/10.1029/2011JD015885, 2011.

Sato, K., Okamoto, H., Yamamoto, M. K., Fukao, S., Kumagai, H., Ohno, Y., Horie, H., and Abo, M.: 95-GHz Doppler radar and lidar synergy for simultaneous ice microphysics and in-cloud vertical air motion retrieval, J. Geophys. Res., 114, D03203, https://doi.org/10.1029/2008JD010222, 2009.

Sato, K., Okamoto, H., Nishizawa, T., Jin, Y., Nakajima, T. Y., Wang, M., Satoh, M., Roh, W., Ishimoto, H., and Kudo, R.: JAXA Level 2 cloud and precipitation microphysics retrievals based on EarthCARE radar, lidar, and imager: the CPR_CLP, AC_CLP, and ACM_CLP products, Atmos. Meas. Tech., 18, 1325–1338, https://doi.org/10.5194/amt-18-1325-2025, 2025.

Seeley, J. T., Jeevanjee, N., Langhans, W., and Romps, D. M.: Formation of Tropical Anvil Clouds by Slow Evaporation, Geophys. Res. Lett., 46, 492–501, https://doi.org/10.1029/2018GL080747, 2019.

Seiki, T., Horie, H., Hagihara, Y., Aoki, S., and Noda, A. T.: Global identification of dominant ice-particle growth in cirrus clouds using EarthCARE satellite observations, EGUsphere, 2025, 1–34, https://doi.org/10.5194/egusphere-2025-4819, 2025.

Sherwood, S. C.: On moistening of the tropical troposphere by cirrus clouds, J. Geophys. Res., 104, 11 949–11 960, https://doi.org/10.1029/1999JD900162, 1999.

Sokol, A. B. and Hartmann, D. L.: Tropical Anvil Clouds: Radiative Driving Toward a Preferred State, J. Geophys. Res., 125, e2020JD033 107, https://doi.org/https://doi.org/10.1029/2020JD033107, 2020.

Stephens, G., Winker, D., Pelon, J., Trepte, C., Vane, D., Yuhas, C., L'Ecuyer, T., and Lebsock, M.: CloudSat and CALIPSO within the A-Train: Ten Years of Actively Observing the Earth System, Bull. Amer. Meteor. Soc., 99, 569–581, https://doi.org/10.1175/BAMS-D-16-0324.1, 2018.

Stubenrauch, C. J., Kinne, S., Mandorli, G., Rossow, W. B., Winker, D. M., Ackerman, S. A., Chepfer, H., Di Girolamo, L., Garnier, A., Heidinger, A., Karlsson, K.-G., Meyer, K., Minnis, P., Platnick, S., Stengel, M., Sun-Mack, S., Veglio, P., Walther, A., Cai, X., Young, A. H., and Zhao, G.: Lessons Learned from the Updated GEWEX Cloud Assessment Database, Surv. Geophys., 45, 1999–2048, https://doi.org/10.1007/s10712-024-09824-0, 2024.

Takahashi, H., Luo, Z. J., Stephens, G., and Mulholland, J. P.: Revisiting the Land-Ocean Contrasts in Deep Convective Cloud Intensity Using Global Satellite Observations, Geophys. Res. Lett., 50, e2022GL102 089, https://doi.org/10.1029/2022GL102089, 2023.

Wall, C. J., Norris, J. R., Gasparini, B., Smith, W. L., Thieman, M. M., and Sourdeval, O.: Observational Evidence that Radiative Heating Modifies the Life Cycle of Tropical Anvil Clouds, J. Climate, 33, 8621–8640, https://doi.org/10.1175/JCLI-D-20-0204.1, 2020.

Wehr, T., Kubota, T., Tzeremes, G., Wallace, K., Nakatsuka, H., Ohno, Y., Koopman, R., Rusli, S., Kikuchi, M., Eisinger, M., Tanaka, T., Taga, M., Deghaye, P., Tomita, E., and Bernaerts, D.: The EarthCARE mission – science and system overview, Atmos. Meas. Tech., 16, 3581–3608, https://doi.org/10.5194/amt-16-3581-2023, 2023.